IOP PUBLISHING INVERSE PROBLEMS

Inverse Problems **28** (2012) 035002 (21pp) doi:10.1088/0266-5611/28/3/035002

A mathematical model and inversion procedure for magneto-acousto-electric tomography

Leonid Kunyansky

Department of Mathematics, University of Arizona, Tucson, AZ 85721, USA

E-mail: leonk@math.arizona.edu

Received 10 August 2011, in final form 21 December 2011
Published 3 February 2012
Online at stacks.iop.org/IP/28/035002

Abstract

Magneto-acousto-electric tomography (MAET), also known as the Lorentz force or Hall effect tomography, is a novel hybrid modality designed to be a high-resolution alternative to the unstable electrical impedance tomography. In this paper, we analyze the existing mathematical models of this method, and propose a general procedure for solving the inverse problem associated with the MAET. It consists in applying to the data one of the algorithms of thermo-acoustic tomography, followed by solving the Neumann problem for the Laplace equation and the Poisson equation. For the particular case when the region of interest is a cube, we present an explicit series solution resulting in a fast reconstruction algorithm. As we show, both analytically and numerically, the MAET is a stable technique yielding high-resolution images even in the presence of significant noise in the data.

Introduction

Magneto-acousto-electric tomography (MAET) is based on the measurements of the electrical potential arising when an acoustic wave propagates through a conductive medium placed in a constant magnetic field [26, 34]. The interaction of the mechanical motion of the free charges (ions and/or electrons) with the magnetic field results in the Lorentz force that causes separation of charges and, thus, generates Lorentz currents within the tissue. The goal of MAET coincides with that of electrical impedance tomography (EIT): to reconstruct the conductivity of the tissue from the values of the electric potential measured on the boundary of the object. The EIT is a fast, inexpensive and harmless modality, which is potentially very valuable due to the large contrast in conductivity between healthy and cancerous tissues [5, 6, 9]. Unfortunately, the reconstruction problems arising in EIT are known to be exponentially unstable.

MAET is one of the several recently introduced hybrid imaging techniques designed to stabilize the reconstruction of electrical properties of tissues by coupling together ultrasound waves with other physical phenomena. Perhaps the best known examples of hybrid methods

are thermo-acoustic tomography (TAT) [16] and the closely related photo-acoustic modality [15, 29]. In the latter methods, the amount of electromagnetic energy absorbed by the medium is reconstructed from measurements (on the surface of the object) of acoustic waves caused by thermo-acoustic expansion (see, e.g., [17, 33]). Another hybrid technique, designed to overcome the instability of EIT is acousto-electric impedance tomography (AEIT) [36]. It couples acoustic waves and electrical currents, through the electro-acoustic effect (see [25]). Although AEIT has been shown, both theoretically and in numerical simulations, to be stable and capable of yielding high-resolution images [3, 8, 18, 19], the feasibility of practical reconstructions is still in question due to the weakness of the acousto-electric effect.

In this paper, we analyze MAET, a modality designed to stably reconstruct the conductivity by combining the magnetic field, acoustic excitation and electric measurements, coupled through the Lorentz force. The physical foundations of MAET were established in [26] and [34]. It was shown in [26] that if a tissue with conductivity $\sigma(x)$ moves with velocity $V(x,t)$ within the constant magnetic field B, the arising Lorentz force will generate the Lorentz currents $J_L(x,t)$ given by the following formula:

$$J_L(x,t) = \sigma(x)B \times V(x,t). \tag{1}$$

Originally, it was proposed to utilize a focused propagating acoustic pulse to induce the electrical response [26, 34]. In [13], wave packets of a certain frequency were used in a physical experiment to reconstruct the current density in a thin slab of a tissue. Similarly, in [4], the use of a perfectly focused acoustic beam was assumed in a theoretical study and in numerical simulations. However, in the above-quoted works, an accurate mathematical model(s) of such beams was not presented. Moreover, the feasibility of focusing a fixed-frequency acoustic beam at an arbitrary point inside the 3D body is problematic. In a theoretical study [30], the use of plane waves of varying frequencies was proposed instead of beams. This is a more realistic approach; however, the analysis in that work relies on several crude approximations (the conductivity is assumed to be close to 1, and the electric field is approximated by one term in the multipole expansion).

To summarize, the existing mathematical models of measurements in the MAET are of an approximate nature; moreover, some of them contradict others. For example, it was found in [13] that if one uses a pair of electrodes to measure the voltage (difference of the potentials) at two points a and b on the boundary of the body, the result is the integral of the mixed product of three vectors: velocity V, magnetic induction B and the so-called lead current J_{ab} (the current that would flow in the body if the difference of potentials was applied at points a and b). The approximate model in [30] implicitly agrees with this conclusion. However, in [4], it is assumed that if the pulse is focused at point x, the measurements will be proportional to the product of the electric potential $u(x)$ and conductivity $\sigma(x)$. This assumption contradicts the previous models; it also seems to be unrealistic since the potential $u(x)$ is defined up to an arbitrary constant, while the measurements are completely determined by the physics of the problem.

In this paper, we first derive, starting from equation (1), a rigorous and general model of the MAET measurements. Next, we show that if a sufficient number of data are measured, one can reconstruct, almost explicitly and in a stable fashion, the conductivity of the tissue. For general domains, the reconstruction can be reduced to the solution of the inverse problem of TAT followed by the solution of the Neumann problem for the Laplace equation and a Poisson equation. In the simpler case of a rectangular domain, the reconstruction formulas can be made completely explicit and the solution is obtained by summing several Fourier series. In the latter case, the algorithm is fast, i.e. it runs in $O(n^3 \log n)$ floating-point operations on an $n \times n \times n$ grid. The results of numerical simulations show that high-resolution images of

the conductivity can be stably recovered from MAET measurements even in the presence of significant noise.

1. Formulation of the problem

Suppose that the object of interest whose conductivity $\sigma(x)$ that we would like to recover is supported within an open and bounded region Ω with the boundary $\partial\Omega$. For simplicity, we will assume that $\sigma(x)$ is smooth in Ω, does not approach 0 and equals 1 in the vicinity of $\partial\Omega$; the support of $\sigma(x) - 1$ lies in some $\Omega_1 \subset \Omega$ and the distance between Ω_1 and $\partial\Omega$ is nonzero. The object is placed in the magnetic field with a constant magnetic induction B and an acoustic wave generated by a source lying outside Ω propagates through the object with the velocity $V(x,t)$. The Lorentz force induces currents $J_L(x,t)$ in Ω given by equation (1). We assume that the electrical interactions occur on a much faster timescale than the mechanical ones, and so all currents and electric potentials depend on t only as a parameter. In addition to the Lorentz currents, the arising electrical potential $u(x,t)$ generates the secondary, Ohmic currents $J_O(x,t)$ given by Ohm's law

$$J_O(x,t) = \sigma(x)\nabla u(x,t).$$

Since there are no sinks or sources of charges in Ω, the total current is divergence free

$$\nabla \cdot (J_L + J_O) = 0.$$

Thus,

$$\nabla \cdot \sigma \nabla u = -\nabla \cdot (\sigma B \times V). \tag{2}$$

Since there are no currents through the boundary, the normal component of the total current $J_L(x,t) + J_O(x,t)$ vanishes:

$$\frac{\partial}{\partial n} u(z) = -(B \times V(z)) \cdot n(z), \qquad z \in \partial\Omega, \tag{3}$$

where $n(z)$ is the exterior normal to $\partial\Omega$ at point z.

We will assume that the boundary values of the potential $u(z,t)$ can be measured at all points z lying on $\partial\Omega$. We will model the measurements by integrating $u(z,t)$ with a weight $I(z)$, thus forming the measuring functional M defined by the formula

$$M(t) = \int_{\partial\Omega} I(z)u(z,t)\,\mathrm{d}A(z), \tag{4}$$

where $A(z)$ is the standard area element. The weight $I(z)$ can be a function or a distribution, subject to the only restriction that its integral over $\partial\Omega$ equals zero. In particular, if one chooses to use $I(z) = \delta(z-a) - \delta(z-b)$, where $\delta(\cdot)$ is the 2D Dirac delta function, then M models the two-point measuring scheme utilized in [13] and [30].

In order to understand what kind of information is encoded in the values of $M(t)$, let us consider the solution $w_I(x)$ of the following divergence equation:

$$\nabla \cdot \sigma \nabla w_I(x) = 0, \tag{5}$$

$$\frac{\partial}{\partial n} w_I(z) = I(z), \qquad z \in \partial\Omega. \tag{6}$$

(To ensure the uniqueness, we will require that the integral of $w_I(z)$ over Ω vanishes.) Then, $w_I(x)$ equals the electric potential that would be induced in the tissue by injecting currents $I(z)$ through $\partial\Omega$. Let us denote the corresponding currents $\sigma\nabla w_I(x)$ by $J_I(x)$:

$$J_I(x) = \sigma \nabla w_I(x). \tag{7}$$

Let us now apply the second Green's identity to the functions $u(x,t)$, $w_I(x)$ and $\sigma(x)$:

$$\int_\Omega [w_I \nabla\cdot(\sigma\nabla u) - u\nabla\cdot(\sigma\nabla w_I)]\,dx = \int_{\partial\Omega} \sigma\left[w_I\frac{\partial}{\partial n}u - u\frac{\partial}{\partial n}w_I\right] dA(z). \tag{8}$$

By taking into account (3), (2), (5) and (6), equation (8) can be simplified to

$$-\int_\Omega w_I \nabla\cdot(\sigma B\times V)\,dx = \int_{\partial\Omega}\sigma w_I\frac{\partial}{\partial n}u\,dA(z) - M(t). \tag{9}$$

By integrating the left-hand side of (9) by parts and by replacing $\frac{\partial}{\partial n}u$ with (3), one obtains

$$\int_\Omega \sigma\nabla w_I\cdot(B\times V)\,dx - \int_{\partial\Omega} w_I\sigma(B\times V)\cdot n\,dA(z) = -\int_{\partial\Omega}\sigma w_I(B\times V)\cdot n\,dA(z) - M(t),$$

$$M(t) = -\int_\Omega \sigma\nabla w_I\cdot(B\times V)\,dx = -\int_\Omega J_I\cdot(B\times V)\,dx = B\cdot\int_\Omega J_I(x)\times V(x,t)\,dx. \tag{10}$$

(Equation (1) in [13] is the particular case of (9) for $I(z)=\delta(z-a)-\delta(z-b)$.)

It is clear from equation (10) that MAET measurements recover some information about currents $J_I(x)$. Let us assume that the speed of sound c and the density ρ of the tissues are approximately constant (as in breast imaging, one of the most important potential applications). Then, the acoustic pressure $p(x,t)$ satisfies the wave equation in Ω:

$$\frac{1}{c^2}\frac{\partial^2}{\partial t^2}p(x,t) = \Delta p(x,t). \tag{11}$$

Additionally, $p(x,t)$ is the time derivative of the velocity potential $\varphi(x,t)$ (see, for example, [10]) so that

$$\begin{aligned} V(x,t) &= \frac{1}{\rho}\nabla\varphi(x,t),\\ p(x,t) &= \frac{\partial}{\partial t}\varphi(x,t). \end{aligned} \tag{12}$$

(The velocity potential $\varphi(x,t)$ also satisfies the wave equation (11).)

Now, by taking into account (12), equation (10) can be re-written as

$$M(t) = \frac{1}{\rho}B\cdot\int_\Omega J_I(x)\times\nabla\varphi(x,t)\,dx.$$

Furthermore, by noting that $\nabla\times(\varphi J_I) = -J_I\times\nabla\varphi + \varphi\nabla\times J_I$, we obtain

$$\begin{aligned} M(t) &= \frac{1}{\rho}B\cdot\left[-\int_\Omega \nabla\times(\varphi J_I)\,dx + \int_\Omega \varphi(x,t)\nabla\times J_I(x)\,dx\right]\\ &= \frac{1}{\rho}B\cdot\left[\int_{\partial\Omega}\varphi(z,t)J_I(z)\times n(z)\,dA(z) + \int_\Omega\varphi(x,t)\nabla\times J_I(x)\,dx\right]. \end{aligned} \tag{13}$$

In some situations, the above equations can be further simplified. For example, if at some moment of time t, the velocity potential $\varphi(x,t)$ vanishes on the boundary $\partial\Omega$, then the surface integral in (13) also vanishes:

$$M(t) = \frac{1}{\rho}B\cdot\int_\Omega\varphi(x,t)\nabla\times J_I(x)\,dx. \tag{14}$$

Similarly, if the boundary $\partial\Omega$ is located far away from the support of inhomogeneity of $\sigma(x)$, the surface integral in (13) can be neglected and we again obtain equation (14).

Equation (13) is our mathematical model of the MAET measurements. Our goal is to reconstruct from the data $M(t)$ the conductivity $\sigma(x)$—by varying B, $\varphi(x,t)$ and $I(z)$. Our strategy for solving this problem is outlined in the following sections. However, some conclusions can be reached just by looking at equation (13). For example, one can note that

if three sets of measurements are conducted with magnetic induction pointing, respectively, in the directions of canonical basis vectors e_1, e_2 and e_3, one can easily reconstruct the sum of integrals in the brackets in (13). Furthermore, if one focuses $\varphi(x,t)$ so that at the moment $t=0$, it becomes the Dirac δ-function centered at y, i.e.

$$\varphi(x,0)=\delta(x-y),$$

then one immediately obtains the value of $\nabla\times J_I$ at point y (such a focusing is theoretically possible as explained in the next section). Thus, by moving the focusing point through the object, one can reconstruct the curl of J_I in all of Ω.

Our model also explains the observation reported in [13] that no signal is obtained when the acoustic wave packet is passing through the regions of constant $\sigma(x)$. In such regions, the current field J_I is irrotational, and therefore, the integral in (14) vanishes.

Finally, it becomes clear that an accurate image reconstruction is impossible if monochromatic acoustic waves of only a single frequency k are used for scanning, no matter how well they are focused. In this case, the spatial component ψ of $\varphi(x,t)=\psi(x)\exp(ikt)$ is a solution of the Helmholtz equation:

$$\Delta\psi+k^2\psi=0$$

and can be approximated in Ω by the plane waves $e^{i\lambda\cdot x}$ with $|\lambda|=k$. Let us assume for simplicity that the electrical boundary is removed to infinity. Then, measuring data $M(t)$ given by (14) is equivalent to collecting values of the Fourier transform of $\nabla\times J_I(x)$ corresponding to the wave vectors λ lying on the sphere $|\lambda|=k$ in the Fourier domain. All the other spatial frequencies cannot be recovered.

2. Reconstructing the curls of currents

The first step toward solving the inverse problem of MAET is the reconstruction of the curls of currents $J_I(x)$ corresponding to certain choices of $I(z)$. Let us assume that all the measurements are repeated three times, with the magnetic induction B pointing, respectively, in the directions of canonical basis vectors e_1, e_2 and e_3. Then, as mentioned above, if $\varphi(x,0)=\delta(x-y)$, one readily recovers from the data $M(0)$ the curl of the current at y, i.e. $\nabla\times J_I(y)$. Generating such a velocity potential is possible at least theoretically. For example, if one simultaneously propagates plane waves $\varphi_\lambda(x,t)=\exp(i\lambda\cdot x-i|\lambda|t)$ with all possible wave vectors λ, the combined velocity potential at the moment $t=0$ will add up to the Dirac delta function $\delta(x)$. Such an arrangement is rather impractical. First, the sources of sound would have to be removed far from the object to produce a good approximation to plane waves within the object. Second, they would have to completely surround the object. Finally, all the sources would have to be synchronized. A variation of this approach is to place small point-like sources in the vicinity of the object. Then, instead of plane waves, propagating spherical fronts (or monochromatic waves) would be generated. These types of waves can also be focused into a delta function (a discussion of such focusing can be found in [19]).

2.1. Synthetic focusing

However, a more practical approach is to utilize some realistic measuring configuration (e.g. one consisting of one or several small sources scanning the boundary sequentially), and then to synthesize algorithmically from the realistic data the desired measurements that correspond to the delta-like velocity potential. Such a *synthetic focusing* was first introduced in the context of hybrid methods in [18, 19, 24]. It was shown, in applications to AET and to the

acoustically modulated optical tomography, that synthetic focusing is equivalent to solving the inverse problem of TAT. The latter problem has been studied extensively and a wide variety of methods is known by now (see reviews [17, 33] and references therein). The same technique can be applied to the MAET as explained below.

2.1.1. Measuring functionals solve the wave equation. Consider a propagating spherical front originated at point y. If the initial conditions on $p_y(x,t)$ are

$$\begin{cases} p_y(x,0) = \delta(x-y), \\ \dfrac{\partial}{\partial t} p_y(x,0) = 0, \end{cases}$$

then $p_y(x,t)$ can be represented in the whole of $\mathbb{R}^3$ by means of the Kirchhoff formula [32]

$$p_y(x,t) = \frac{\partial}{\partial t}\frac{\delta(|x-y|-ct)}{4\pi|x-y|}.$$

Such a front can be generated by a small transducer placed at y and excited by a delta-like electric pulse; such devices are common in ultrasonic imaging.

The velocity potential $\varphi(x,y,t)$ corresponding to $p_y(x,t)$ then equals

$$\varphi(x,y,t) = \frac{\delta(|x-y|-ct)}{4\pi|x-y|}. \tag{15}$$

The role of variables x and y is clearly interchangeable; $\varphi(x,y,t)$ is the retarded Green's function of the wave equation [32] either in x and t, or in y and t. Moreover, consider the following convolution $H(y,t)$ of a finitely supported smooth function $h(y)$ with φ

$$H(y,t) = \int_{\mathbb{R}^3} h(y)\frac{\delta(|x-y|-ct)}{4\pi|x-y|}\,\mathrm{d}x.$$

Then, $H(y,t)$ is the solution of the following initial value problem (IVP) in $\mathbb{R}^3$ [32]:

$$\begin{cases} \dfrac{1}{c^2}\dfrac{\partial^2}{\partial t^2}H(y,t) = \Delta_y H(y,t), \\ H(y,0) = 0, \\ \dfrac{\partial}{\partial t}H(y,0) = h(y). \end{cases} \tag{16}$$

Now suppose that a set of MAET measurements is obtained with propagating wave fronts $\varphi(x,y,t)$ with different centers y (while $I(z)$ and B are kept fixed). By substituting (15) into (13), we find that, for each y, the corresponding measuring functional $M_{I,B}(y,t)$ can be represented as the sum of two terms:

$$M_{I,B}(y,t) = M^{\mathrm{sing}}_{I,B}(y,t) + M^{\mathrm{reg}}_{I,B}(y,t),$$

where

$$M^{\mathrm{sing}}_{I,B}(y,t) = \frac{1}{\rho}\int_{\partial\Omega}\frac{\delta(|z-y|-ct)}{4\pi|z-y|}B\cdot J_I(z)\times n(z)\,\mathrm{d}A(z), \tag{17}$$

$$M^{\mathrm{reg}}_{I,B}(y,t) = \frac{1}{\rho}\int_{\Omega}\frac{\delta(|x-y|-ct)}{4\pi|x-y|}B\cdot\nabla\times J_I(x)\,\mathrm{d}x. \tag{18}$$

It is clear from the above discussion that both terms $M^{\mathrm{sing}}_{I,B}(y,t)$ and $M^{\mathrm{reg}}_{I,B}(y,t)$ solve the wave equation in $\mathbb{R}^3$, subject to the initial conditions

$$\frac{\partial}{\partial t}M^{\mathrm{sing}}_{I,B}(x,0) = \frac{1}{\rho}B\cdot J_I(x)\times n(x)\delta_{\partial\Omega}(x), \tag{19}$$

$$\frac{\partial}{\partial t} M^{\text{reg}}_{I,B}(x,0) = \frac{1}{\rho} B \cdot \nabla \times J_I(x), \tag{20}$$

$$M^{\text{sing}}_{I,B}(y,0) = M^{\text{reg}}_{I,B}(y,0) = 0, \tag{21}$$

where $\delta_{\partial\Omega}(x)$ is the delta function supported on $\partial\Omega$. While the singular term $M^{\text{sing}}_{I,B}(y,t)$ solves the wave equation in the sense of distributions, the regular term $M^{\text{reg}}_{I,B}(y,t)$ represents a classical solution of the wave equation.

Proposition 1. *Suppose the conductivity $\sigma(x)$ and boundary currents $I(z)$ are the C^∞ functions of their arguments and the boundary $\partial\Omega$ is infinitely smooth. Then, the regular part $M^{\text{reg}}_{I,B}(y,t)$ of the measuring functional is a C^∞ solution of the wave equation*

$$\frac{1}{c^2}\frac{\partial^2}{\partial t^2} M^{\text{reg}}_{I,B}(y,t) = \Delta_y M^{\text{reg}}_{I,B}(y,t), \qquad y \in \mathbb{R}^3, \qquad t \in [0,\infty), \tag{22}$$

satisfying initial conditions (20) and (21).

Proof. Under the above conditions, the potential $w_I(x)$ solving the boundary value problem (5), (6) is a C^∞ function in Ω due to the classical estimates on the smoothness of solutions of elliptic equations with smooth coefficients [12]. The curl of J_I vanishes outside of Ω_1 since $\sigma(x)$ is constant in $\Omega\backslash\Omega_1$. Therefore, the right-hand side of (20) can be extended by zero to a C^∞ function in $\mathbb{R}^3$. The term $M^{\text{reg}}_{I,B}(y,t)$ defined by equation (18) solves wave equation (22) (due to the Kirchhoff formula [32]) subject to infinitely smooth initial conditions (20) and (21), and thus, it is a C^∞ function for all $y \in \mathbb{R}^3, t \in [0,\infty)$. □

2.1.2. Reconstructing the initial conditions. We would like to reconstruct the right-hand side of (20) (and possibly that of (19)) from the measured values of $M_{I,B}(y,t)$. Since c is assumed constant, in the 3D case, $M_{I,B}(y,t)$ will vanish (due to the Huygens principle) for $t > t_{\max} = D_{\max}/c$, where $D_{\max}$ is the maximal distance between the points of Ω and the acoustic sources. We will assume that $M_{I,B}(y,t)$ is measured for all $t \in [0, t_{\max}]$.

The problem of reconstructing $\frac{\partial}{\partial t} M_{I,B}(x,0)$ from $M_{I,B}(y,t)$ is equivalent to that of reconstructing the initial value $h(y)$ from the solution of IVP (16). The latter, a more general problem, has been studied extensively in the context of TAT (see e.g. [17, 33] and references therein). In the case of TAT, points y describe the location of detectors rather than sources, but the rest of the mathematics remains the same. The most-studied situation is when the detectors are placed on a closed surface Σ surrounding the object. If Σ is a sphere, a variety of inversion techniques is known, including (but not limited to) the explicit inversion formulas [11, 20, 28], series techniques [21, 23, 27, 35], time reversal by means of finite differences [2, 7, 14], etc. If Σ is a surface of a cube, one can use the inversion formula [22], the already-mentioned time-reversal methods or the fast algorithm developed in [21] for such surfaces.

The choice of the TAT inversion method for the application in the MAET will depend, in particular, on the mutual location of the electric boundary $\partial\Omega$ and the acoustic source surface Σ. One can decide to move the electric boundary further away by placing the object in a liquid with conductivity equal to 1 and by submerging the acoustic sources into the liquid, in which case Σ will be inside $\partial\Omega$. Alternatively, one can move the acoustic surface further away so that it surrounds the electric boundary. Finally, one may choose to conduct the electrical measurements on the surface of the body and to place the acoustic sources on the same surface, in which case Σ will coincide with $\partial\Omega$.

If $\partial\Omega$ lies inside Σ, all the above-mentioned TAT inversion techniques (theoretically) will reconstruct both $\frac{\partial}{\partial t} M^{\text{sing}}_{I,B}(y,0)$ and $\frac{\partial}{\partial t} M^{\text{reg}}_{I,B}(y,0)$. In practice, accurate numerical reconstruction

of the singular term $\frac{\partial}{\partial t}M^{\text{sing}}_{I,B}(y,0)$ supported on $\partial\Omega$ may be difficult to obtain due to the finite resolution of any realistic measurement system. Luckily, the support Ω_1 of $\frac{\partial}{\partial t}M^{\text{reg}}_{I,B}(y,0)$ is spatially separated from $\partial\Omega$, so that the contributions from the singular term can be eliminated just by setting the reconstructed image to zero outside Ω_1 . As explained further in this paper, $\frac{\partial}{\partial t}M^{\text{reg}}_{I,B}(y,0)$ contains enough information to reconstruct the conductivity. On the other hand, $\frac{\partial}{\partial t}M^{\text{sing}}_{I,B}(y,0)$ does carry some useful information, which can be recovered by a specialized reconstruction algorithm.

If Σ lies inside $\partial\Omega$ (but Ω_1 still lies inside Σ), not all TAT reconstruction techniques can be applied. Most of the inversion formulas will produce an incorrect result in the presence of exterior sources (such as the term $\frac{\partial}{\partial t}M^{\text{sing}}_{I,B}(y,0)$ supported on $\partial\Omega$ and exterior with respect to the region enclosed by Σ). On the other hand, formula [22], series methods [1,21] and all the time-reversal techniques automatically filter out the exterior sources and, thus, can be used to reconstruct $\frac{\partial}{\partial t}M^{\text{reg}}_{I,B}(y,0)$.

The situation is more complicated if surfaces Σ and $\partial\Omega$ coincide. However, those methods that are insensitive to sources located outside $\partial\Omega$ are also insensitive to the sources located on $\partial\Omega$, particularly to those represented by $\frac{\partial}{\partial t}M^{\text{sing}}_{I,B}(y,0)$. These methods can be used to reconstruct $\frac{\partial}{\partial t}M^{\text{reg}}_{I,B}(y,0)$. In other words, the following proposition holds.

Proposition 2. *If values of the measuring functional $M_{I,B}(y,t)$ are known for all $y \in \Sigma$ and $t \in [0, D_{\max}/c]$, the term $\frac{\partial}{\partial t}M^{\text{reg}}_{I,B}(y,0)$ can be exactly reconstructed in Ω_1 (by using one of the above-mentioned TAT algorithms). Moreover, if the conditions of proposition 1 are satisfied, the reconstruction is exact pointwise.*

In order to reconstruct the curl of the current $J_I(x)$, we need to repeat the procedure of finding $\frac{\partial}{\partial t}M^{\text{reg}}_{I,B}(x,0)$ three times, with three different orientations of B : $B^{(j)} = |B|e_j$, $j = 1, 2, 3$. As a result, we find the projections of $\nabla \times J_I(x)$ on all e_j's and thus obtain

$$\nabla \times J_I(x) = \frac{\rho}{|B|}\sum_{j=1}^{3} e_j \frac{\partial}{\partial t}M^{\text{reg}}_{I,B^{(j)}}(x,0), \qquad x \in \Omega_1. \tag{23}$$

(outside Ω_1, the curl of $J_I(x)$ equals 0 since $\sigma(x)$ is constant in $\Omega\backslash\Omega_1$).

If, in addition, $\partial\Omega$ lies inside Σ and $\frac{\partial}{\partial t}M^{\text{sing}}_{I,B}(y,0)$ has been recovered, we also obtain

$$J_I(x) \times n(x)\delta_{\partial\Omega}(x) = \frac{\rho}{|B|}\sum_{j=1}^{3} e_j \frac{\partial}{\partial t}M^{\text{sing}}_{I,B^{(j)}}(x,0). \tag{24}$$

3. Reconstructing currents from the curls

The considerations of the previous section show how to recover from the values of the measuring functionals $M_{I,B^{(j)}}(y,t)$, the curl of J_I and, in some situations, the surface term (24). The next step is to reconstruct the current J_I.

We know that J_I satisfies the following boundary conditions:

$$J_I \cdot n|_{\partial\Omega} = \frac{\partial}{\partial n}w_I\bigg|_{\partial\Omega} = I. \tag{25}$$

In certain simple domains, one can find a way to solve the equation

$$C = \nabla \times J_I$$

for J_I in such a way that conditions (25) are satisfied automatically. One such domain is a cube; we present the corresponding algorithm in section 5. In general, however, a solution of an auxiliary Neumann problem may be needed as discussed below.

Let us start with the most general situation and assume that only the curl $C = \nabla \times J_I$ has been reconstructed. Since the current J_I is a purely solenoidal field whose curl vanishes on $\partial\Omega$, there exists a vector potential $K(x)$, such that

$$J_I(x) = \nabla \times K(x) + \Psi(x), \qquad x \in \Omega, \tag{26}$$

where $K(x)$ has the form

$$K(x) = \int_\Omega \frac{C(y)}{4\pi|x-y|}\,\mathrm{d}y,$$

and $\Psi(x)$ is both a solenoidal and a potential field within Ω. Then, there exists a harmonic potential $\psi(x)$, such that $\Psi(x) = \nabla\psi(x)$. Therefore, by combining equations (26) and (25), one obtains

$$\left(n \cdot (\nabla \times K)(z) + \frac{\partial}{\partial n}\psi(z)\right)\Big|_{\partial\Omega} = I(z),$$

and $\psi(z)$ now can be recovered by solving the Neumann problem

$$\begin{cases} \Delta\psi(x) = 0, & x \in \Omega \\ \dfrac{\partial}{\partial n}\psi(z) = I(z) - n \cdot \left(\nabla \times \displaystyle\int_\Omega \frac{C(y)}{4\pi|z-y|}\,\mathrm{d}y\right), & z \in \partial\Omega. \end{cases} \tag{27}$$

Now, $J_I(x)$ is uniquely defined by the formula

$$J_I(x) = \nabla \times \int_\Omega \frac{C(y)}{4\pi|x-y|}\mathrm{d}y + \nabla\psi(x), \qquad x \in \Omega. \tag{28}$$

Proposition 3. *Under the smoothness assumptions of proposition 1, current $J_I(x)$ is given by (28), where the function $\psi(x)$ is the (classical) solution of the Neumann problem (27).*

If, in addition to the curl $\nabla \times J_I(x)$, the surface term (equation (24)) has been reconstructed, there is no need to solve the Neumann problem. Instead, the function $\Psi(x)$ is given explicitly by the following formula [31]:

$$\Psi(x) = \nabla_x \times \int_{\partial\Omega} \frac{J_I(y) \times n(y)}{4\pi|x-y|}\mathrm{d}A(y).$$

The final expression for current J_I can now be written as

$$\begin{aligned} J_I(x) &= \nabla_x \times \left[\int_\Omega \frac{C(y)}{4\pi|x-y|}\mathrm{d}y + \int_{\partial\Omega} \frac{J_I(y) \times n(y)}{4\pi|x-y|}\,\mathrm{d}A(y)\right] \\ &= \nabla_x \times \int_{\bar\Omega} \frac{C(y) + J_I(y) \times n(y)\delta_{\partial\Omega}(y)}{4\pi|x-y|}\,\mathrm{d}y, \quad x \in \Omega, \end{aligned} \tag{29}$$

where $\bar\Omega$ is the closure Ω. The term with the delta function in the numerator of (29) coincides with the surface term (24). In order to avoid the direct numerical reconstruction of the singular term, one may want to try to modify the utilized TAT reconstruction algorithm so as to recover directly the convolution with $\frac{1}{4\pi|x|}$ contained in equation (29). The practicality of such an approach requires further investigation.

4. Reconstructing conductivity from the currents

In order to reconstruct $\sigma(x)$, we utilize three currents $J^{(k)}$, $k = 1, 2, 3$, corresponding to different boundary conditions I_k. We also use three different magnetic inductions $B^{(j)}$, $j = 1, 2, 3$, and, as a result, obtain the values of the following measuring functionals:

$$M_{I_k,B^{(j)}}(y,t) = \int_{\partial\Omega} I_k(z)u_{(j)}(z,t)\,\mathrm{d}A(z), \qquad j = 1,2,3, \qquad k = 1,2,3, \tag{30}$$

where $u_{(j)}(z,t)$ is the electric potential corresponding to the acoustic wave with the velocity potential $\varphi(x,z,t)$ propagating through the body in the presence of constant magnetic field $B^{(j)}$. The increase in the number of currents $J^{(k)}$ does not require additional physical measurements: the same measured boundary values of $u_{(j)}(z,t)$ are used to compute different functionals by changing the integration weight $I_k(z)$ in (4).

For each of the currents $J^{(k)}$, we apply one of the above-mentioned TAT reconstruction techniques to compute $\frac{\partial}{\partial t}M_{I_k,B^{(j)}}(y,0)$. The knowledge of the latter functions for $B^{(j)}$, $j=1,2,3$, allows us to recover the curls $C^{(k)}=\nabla\times J^{(k)}$, $k=1,2,3$, (equation (23)) and, possibly, the surface terms (24). Finally, currents $J^{(k)}$ are reconstructed by one of the methods described in the previous section.

At the first sight, finding $\sigma(x)$ from the knowledge of $J^{(k)}=\sigma\nabla w_{I_k}$, $k=1,2,3$, is a nonlinear problem, since the unknown electric potentials w_{I_k} depend on $\sigma(x)$. However, as shown below, this problem can be solved explicitly without linearization or some other approximation. Indeed, for any $k=1,2,3$, the following formula holds:

$$0=\nabla\times\frac{J^{(k)}}{\sigma}=\left(\nabla\frac{1}{\sigma}\right)\times J^{(k)}+\frac{1}{\sigma}C^{(k)}=-\frac{1}{\sigma^2}(\nabla\sigma)\times J^{(k)}+\frac{1}{\sigma}C^{(k)}$$

so that

$$\nabla\ln\sigma(x)\times J^{(k)}(x)=C^{(k)}(x),\qquad x\in\Omega,\qquad k=1,2,3. \tag{31}$$

Now, one can try to find $\nabla\ln\sigma$ at each point in Ω by solving the (in general) over-determined system of linear equations (31).

Let us assume first, that at each point x in Ω, the currents $J^{(l)}(x)$, $l=1,2,3$, form a basis in $\mathbb{R}^3$. There are nine equations in system (31), whose unknowns are the three components of $\nabla\ln\sigma$, but the rank of the corresponding matrix does not exceed 6. In order to see this, let us multiply each equation of (31) by $J^{(l)}$, $l=1,2,3$. (Since currents $J^{(l)}$ form a basis, this is equivalent to a multiplication by a non-singular matrix.) We obtain

$$\begin{cases}\nabla\ln\sigma\cdot(J^{(1)}\times J^{(2)})=C^{(1)}\cdot J^{(2)}\\ \nabla\ln\sigma\cdot(J^{(1)}\times J^{(2)})=-C^{(2)}\cdot J^{(1)}\\ \nabla\ln\sigma\cdot(J^{(1)}\times J^{(3)})=C^{(1)}\cdot J^{(3)}\\ \nabla\ln\sigma\cdot(J^{(1)}\times J^{(3)})=-C^{(3)}\cdot J^{(1)}\\ \nabla\ln\sigma\cdot(J^{(2)}\times J^{(3)})=C^{(2)}\cdot J^{(3)}\\ \nabla\ln\sigma\cdot(J^{(2)}\times J^{(3)})=-C^{(3)}\cdot J^{(2)}.\end{cases}$$

In the absence of noise, the right-hand sides of equations (2), (4) and (6) in the above system would coincide with those of equations (1), (3) and (5), respectively, and therefore, three equations could be dropped from the system. However, in order to reduce the noise sensitivity of the method, we average the equations with identical left-hand sides (this is equivalent to finding the least-squares solution of this system). We thus obtain

$$\begin{cases}\nabla\ln\sigma\cdot(J^{(1)}\times J^{(2)})=R_1, & R_1=\frac{1}{2}(C^{(1)}\cdot J^{(2)}-C^{(2)}\cdot J^{(1)}),\\ \nabla\ln\sigma\cdot(J^{(1)}\times J^{(3)})=R_2, & R_2=\frac{1}{2}(C^{(1)}\cdot J^{(3)}-C^{(3)}\cdot J^{(1)}),\\ \nabla\ln\sigma\cdot(J^{(2)}\times J^{(3)})=R_3, & R_3=\frac{1}{2}(C^{(2)}\cdot J^{(3)}-C^{(3)}\cdot J^{(2)}).\end{cases} \tag{32}$$

As shown in the appendix, the solution of (32) can be written explicitly as follows:

$$\nabla\ln\sigma=\frac{1}{J^{(1)}\cdot(J^{(2)}\times J^{(3)})}A\mathbf{R}, \tag{33}$$

where $\mathbf{R}=(R_3,-R_2,R_1)^T$ and A is a 3×3 matrix whose columns are the Cartesian coordinates of the currents $J^{(1)}$, $J^{(2)}$ and $J^{(3)}$, respectively. Since, by assumption, currents $J^{(l)}$ form a basis at each point of Ω, the denominator in (33) never vanishes, and thus, equation (33) can be used to reconstruct $\nabla\ln\sigma$ in all of Ω.

Finally, we compute the divergence of both sides in (33):

$$\Delta \ln \sigma = \nabla \cdot \frac{A\mathbf{R}}{J^{(1)} \cdot (J^{(2)} \times J^{(3)})} \tag{34}$$

and solve the Poisson equation (34) for $\ln \sigma$ in Ω subject to the Dirichlet boundary conditions

$$\ln \sigma|_{\partial\Omega} = 0. \tag{35}$$

The above reconstruction procedure works if currents $J^{(k)}(x)$, $k = 1, 2, 3$, are linearly independent at each $x \in \Omega$. In general, this cannot be guaranteed. There exists a counterexample [8] with such a conductivity and a boundary condition that the corresponding current vanishes at a point within the domain. Such a situation, however, is unlikely to occur for a realistic $\sigma(x)$ and our method should still be useful.

Moreover, the condition of three currents forming a basis at each $x \in \Omega$ can be relaxed. Let us show that if one of the currents (say $J^{(3)}$) vanishes at some x and the two other currents are not parallel in x, the following system is still uniquely solvable:

$$\begin{cases} \nabla \ln \sigma \times J^{(1)} = C^{(1)}, \\ \nabla \ln \sigma \times J^{(2)} = C^{(2)}. \end{cases} \tag{36}$$

Indeed, let us multiply via the dot product the above equations by $J^{(2)}$ and $J^{(1)}$, respectively, and subtract them. We obtain

$$\nabla \ln \sigma \cdot (J^{(1)} \times J^{(2)}) = \tfrac{1}{2}(C^{(1)} \cdot J^{(2)} - C^{(2)} \cdot J^{(1)}). \tag{37}$$

Now, multiply the first equation in (36) by $J^{(1)} \times J^{(2)}$. The left-hand side yields

$$\begin{aligned} (\nabla \ln \sigma \times J^{(1)}) \cdot (J^{(1)} \times J^{(2)}) &= \nabla \ln \sigma \cdot [J^{(1)} \times (J^{(1)} \times J^{(2)})] \\ &= \nabla \ln \sigma \cdot [(J^{(1)} \cdot J^{(2)})J^{(1)} - (J^{(1)} \cdot J^{(1)})J^{(2)}], \end{aligned}$$

which leads to the equation

$$\nabla \ln \sigma \cdot [(J^{(1)} \cdot J^{(2)})J^{(1)} - (J^{(1)} \cdot J^{(1)})J^{(2)}] = C^{(1)} \cdot (J^{(1)} \times J^{(2)}). \tag{38}$$

Similarly, by multiplying the second equation in (36) by $(J^{(2)} \times J^{(1)})$, we obtain

$$\nabla \ln \sigma \cdot [(J^{(1)} \cdot J^{(2)})J^{(2)} - (J^{(2)} \cdot J^{(2)})J^{(1)}] = C^{(2)} \cdot (J^{(2)} \times J^{(1)}). \tag{39}$$

Equations (37)–(39) form a linear system with three equations and three unknowns. This system is solvable since the vectors given in the bracketed expressions in (38) and (39) are not parallel. Indeed, the cross product of these terms yields

$$[\cdots] \times [\cdots] = (J^{(1)} \times J^{(2)})[(J^{(1)} \cdot J^{(2)})^2 - (J^{(1)} \cdot J^{(1)})(J^{(2)} \cdot J^{(2)})].$$

The above expression is clearly nonzero if $J^{(1)}$ and $J^{(2)}$ are not parallel, and therefore, the system of the three equations (37), (38) and (39) is uniquely solvable in this case.

Theorem 4. *Suppose that the conditions of proposition 1 are satisfied and that the conductivity* $\sigma(x)$ *and boundary currents* I_k, $k = 1, 2, 3$, *are such that at each point* $x \in \Omega$, *two of the three correspondent currents* $J^{(k)}$ *are non-parallel. Then, the logarithm of the conductivity* $\ln \sigma$ *is uniquely determined by the values of the measuring functionals* $M_{I_k, B^{(j)}}(y, t)$, $k = 1, 2, 3$, $j = 1, 2, 3$, $y \in \Sigma$ *and* $t \in [0, D_{\max}/c]$.

Proof. By propositions 1–4, from the values of $M_{I_k, B^{(j)}}(y, t)$, one can reconstruct currents $J^{(k)}(x)$, $k = 1, 2, 3$, at each $x \in \Omega$. Since at each x, at least two of the three currents (let us call them $J^{(1)}$ and $J^{(2)}$) are not parallel, the system of the three equations (37), (38) and (39) is uniquely solvable, and $\nabla \ln \sigma$ can be found at each $x \in \Omega$. Since σ is bounded away from zero, $\nabla \ln \sigma$ is a C^∞ function in Ω. By computing the divergence of $\nabla \ln \sigma$, the problem of

finding $\ln\sigma$ reduces to solving the Poisson problem with zero Dirichlet boundary conditions in a smooth domain Ω. □

The condition that out of the three currents two are nonzero and not parallel is less restrictive than the requirement that the three currents are linearly independent. To the best of our knowledge, there exists no counterexample showing that the former condition can be violated, i.e. one of the three currents generated by linearly independent boundary conditions vanishes and the other two are parallel at some point in space. On the other hand, we know of no proof that this cannot happen.

5. The case of a rectangular domain

In the previous sections, we presented a theoretical scheme for finding the currents $J^{(k)}$, $k = 1, 2, 3$, and conductivity $\sigma(x)$ from the MAET measurements in a rather general setting, where the electrical domain Ω and surface Σ supporting the acoustic sources were quite arbitrary. This scheme consists in solving the inverse problem of TAT in the domain surrounded by Σ, the Neumann problem for the Laplace equation in Ω and the Poisson equation for $\ln\sigma$, also in Ω. All these problems are well studied and algorithms for their solution are well known. However, in the case when Ω is a cube and Σ coincides with $\partial\Omega$, the reconstruction can be obtained in the form of an explicit series solution.

5.1. Fast reconstruction algorithm

Let us assume that the domain Ω is a cube $[0, 1] \times [0, 1] \times [0, 1]$ and the sound sources are located on $\partial\Omega$. (In practice, such a configuration will occur if the object is placed in a cubic tank filled with conductive liquid, with the sources of sound and electrodes placed on the tank walls.) We will use three boundary conditions I_k defined by the formulas

$$I_k(x) = \begin{cases} \frac{1}{2}, & x \in \partial\Omega, \quad x_k = 1 \\ -\frac{1}{2}, & x \in \partial\Omega, \quad x_k = 0 \\ 0, & x \in \partial\Omega, \quad 0 < x_k < 1. \end{cases}, \qquad k = 1, 2, 3, \qquad x = (x_1, x_2, x_3). \tag{40}$$

As before, all the measurements are repeated with three different directions of the magnetic field $B^{(j)} = |B|e_j$, $j = 1, 2, 3$, and functionals $M_{I_k,B^{(j)}}(y, t)$ (see equation (30)) are computed from the values of the electrical potentials $u^{(j)}(x, t)$ on $\partial\Omega$, for $t \in \left[0, \frac{\sqrt{3}}{c}\right]$.

We start the reconstruction by applying to $M_{I_k,B^{(j)}}(y, t)$ the fast cubic-domain TAT algorithm [21] to recover the regular terms $\frac{\partial}{\partial t} M^{\text{reg}}_{I^{(k)},B^{(j)}}(x, 0)$, $j = 1, 2, 3$, $k = 1, 2, 3$. (The algorithm we chose automatically sets to zero the sources corresponding to the surface terms $\frac{\partial}{\partial t} M^{\text{sing}}_{I^{(k)},B^{(j)}}(x, 0)$ supported on Σ.) This is done for all three directions of $B^{(j)}$ so that we immediately obtain the curls $C^{(k)}(x) = \nabla \times J^{(k)}(x)$, $k = 1, 2, 3$, $x \in \partial\Omega$.

Now, since the currents are divergence free,

$$\nabla \times C^{(k)}(x) = \nabla \times \nabla \times J^{(k)}(x) = -\Delta J^{(k)}(x).$$

The above equations are a set of Poisson problems for the components of $J^{(k)}$ in Ω. Below, we discuss how to enforce the correct boundary conditions for these problems.

Let us recall that

$$J^{(k)}(x) = \sigma \nabla w^{(k)}(x),$$

where $w^{(k)}$ is the corresponding electric potential. It is convenient to subtract the linear component from potentials, i.e. to introduce $w^{(k),0}(x)$ and $J^{(k),0}(x)$ defined as follows:

$$w^{(k)}(x) = w^{(k),0}(x) + x_k,$$
$$J^{(k)}(x) = J^{(k),0}(x) + e_k, \qquad k = 1, 2, 3.$$

Now, each $w^{(k),0}$ satisfies zero Neumann conditions on $\partial\Omega$ and thus can be extended by even reflections to a periodic function in $\mathbb{R}^3$. Since $w^{(k),0}$ is a harmonic function near $\partial\Omega$, such an extension will be a harmonic function in the neighborhood of $\partial\Omega$. Therefore, each $w^{(k),0}$ can be expanded in the Fourier cosine series in Ω, and the derivatives of this series yield correct behavior of the so-computed $\nabla w^{(k),0}$ and $J^{(k),0}$ on $\partial\Omega$. ($J^{(k),0}$ coincide with $\nabla w^{(k),0}$ in the vicinity of $\partial\Omega$.) Therefore, the components of currents $J^{(k),0}$ should be expanded in the Fourier series whose basis functions are the corresponding derivatives of the cosine series. In other words, the following series yield correct boundary conditions when used as a basis for expanding the currents $J^{(k),0}$, $k = 1, 2, 3$:

$$\begin{cases} J_1^{(k),0}(x) = \displaystyle\sum_{l=1}^{\infty}\sum_{m=0}^{\infty}\sum_{n=0}^{\infty} A_{l,m,n}^{(k),1} \sin \pi l x_1 \cos \pi m x_2 \cos \pi n x_3 \\ J_2^{(k),0}(x) = \displaystyle\sum_{l=0}^{\infty}\sum_{m=1}^{\infty}\sum_{n=0}^{\infty} A_{l,m,n}^{(k),2} \cos \pi l x_1 \sin \pi m x_2 \cos \pi n x_3 \\ J_3^{(k),0}(x) = \displaystyle\sum_{l=0}^{\infty}\sum_{m=0}^{\infty}\sum_{n=1}^{\infty} A_{l,m,n}^{(k),3} \sin \pi l x_1 \cos \pi m x_2 \cos \pi n x_3, \end{cases} \tag{41}$$

where $J^{(k),0}(x) = \left(J_1^{(k),0}(x), J_2^{(k),0}(x), J_3^{(k),0}(x)\right)$. Now, since $\nabla \times J^{(k),0}(x) = \nabla \times J^{(k)}(x)$,

$$\Delta J^{(k),0}(x) = -\nabla \times C^{(k)}(x), \qquad k = 1, 2, 3, \tag{42}$$

and if the Poisson problems (42) are solved for each component of $J^{(k),0}$ using sine/cosine Fourier series (41), the correct boundary conditions will be attained. The computation is fast if the fast Fourier sine and cosine transforms (FFST and FFCT) are utilized.

Note that before the Poisson problems (42) can be solved, the curl of $C^{(k)}$ needs to be computed. This is done by expanding $C^{(k)}$ in the Fourier sine series and by differentiating the series, again using the FFST and FFCT. In other words, we numerically differentiate data that may contain noise. However, this does not give rise to instabilities, since this differentiation is immediately followed by an inverse Laplacian (describing the solution of the Poisson problem) so that the combined operator is actually smoothing.

Finally, once the currents are reconstructed, we form the right-hand side of the system (34) and solve this Poisson problem for $\ln \sigma(x)$ by using the Fourier sine series that yields the desired boundary conditions (35). Again, the FFST and FFCT are utilized here and in the computations of the divergence needed to form equation (34).

All the steps of the present algorithm are explicit and can be performed fast using the FFST and FFCT. The same is true for the TAT reconstruction technique [21] used in the first step so that the required number of floating-point operations (flops) for the whole method is $O(n^3 \ln n)$ for a Cartesian computational grid with n^3 nodes.

5.2. Numerical results

We demonstrate the work of the cubic-domain reconstruction algorithm on simulated data. For the most thorough simulation, we would need to solve equation (2) with the boundary conditions (3) for various propagating fronts $V(x, t)$ centered at different locations on $\partial\Omega$. The number of the modeled data points would need to be similar to the number of unknowns.

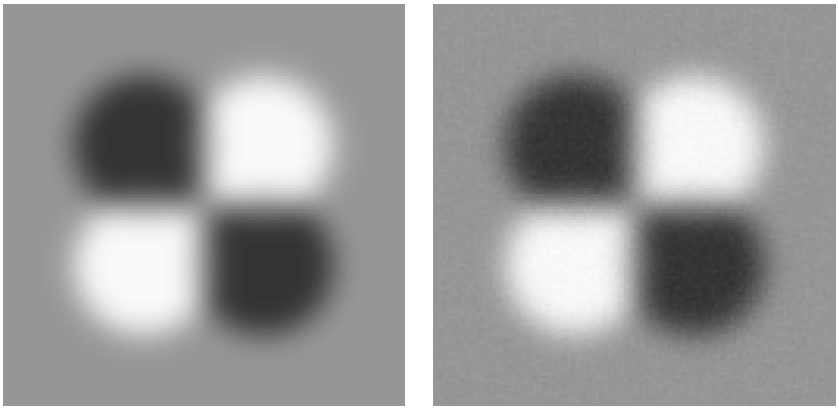

(a) (b)

Figure 1. A 3D simulation with a smooth phantom representing $\ln \sigma(x)$. (a) The cross section of the phantom by the plane $x_3 = 0.5$. (b) Reconstruction from the data with added 50% (in L_2 sense) noise.

For a fine grid (say of the size $257 \times 257 \times 257$), we would have to solve equation (2) several million times. This task is too challenging computationally.

Instead, for a given phantom and for the set of functions $I^{(k)}$ given by (40), we computed currents $J^{(k)}$ by solving equation (5) with boundary conditions (6). Next, the wave equation (16) with the initial condition $h(y) = B^{(j)} \cdot \nabla \times J^{(k)}(x)$ was solved for $j = 1, 2, 3, k = 1, 2, 3$; the solution of this equation at points in $\partial\Omega$ simulated the regular part $\rho M^{\text{reg}}_{I,B}(x, t)$ of the measuring functionals. For simplicity, we did not model the singular term $M^{\text{sing}}_{I,B}(x, t)$ given by (17). Theoretically, when the TAT reconstruction algorithm [21] is applied to such data, this term (not supported in Ω) will not contribute to the reconstruction and simulating it will not bring additional insight.

As the first phantom simulating $\ln \sigma(x)$, we used the following linear combinations of four C^8 radially symmetric functions $\varphi(x - x^{(i)})$:

$$f(x) = \varphi(|x - x^{(1)}|) - \varphi(|x - x^{(2)}|) - \varphi(|x - x^{(3)}|) + \varphi(|x - x^{(4)}|), \qquad (43)$$

where $\varphi(t)$ is a decreasing non-negative trigonometric polynomial on $[0, r_0]$, such that $\varphi(0) = 0.5$, $\varphi(t) = 0$ for $t \geqslant r_0$ and the first eight derivatives of φ vanish at 0 and at r_0; and centers $x^{(i)}$ were lying in the plane $x_3 = 0$: $x^{(1)} = (0.25, 0.25, 0)$, $x^{(2)} = (0.25, 0.75, 0)$, $x^{(3)} = (0.75, 0.25, 0)$, $x^{(4)} = (0.75, 0.75, 0)$. The radius r_0 was equal to 0.34 in this simulation. A grayscale picture of this phantom is shown in figure 1(a). Figure 1(b) demonstrates the cross section by the plane $x_3 = 0.5$ of the image reconstructed on a $129 \times 129 \times 129$ computational grid from simulated data with added noise. The acoustic sources were located at the nodes of 129×129 Cartesian grids on each of the six faces of the cubic domain Ω. For each source, 223 values of each measuring functional were computed, representing 223 different time samples (or 223 radii) of the propagating acoustic front.

The measurement noise was simulated by adding values of a uniformly distributed random variable to the data. The noise was scaled in such a way that for each time series (one source position), the noise intensity in L^2 norm was 50% of the intensity of the signal (i.e. of the L^2 norm of the data sequence representing the measuring functional). In spite of such a high level of noise in the data, the reconstruction shown in figure 1(b) contains very little noise. This can

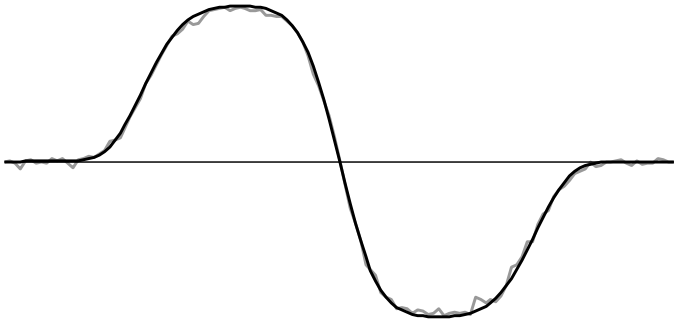

Figure 2. The cross section of the reconstructed image (shown in figure 1) by the line $x_1 = 0.25$, $x_3 = 0.5$. The thick black line represents the phantom and the gray line corresponds to the reconstructed image.

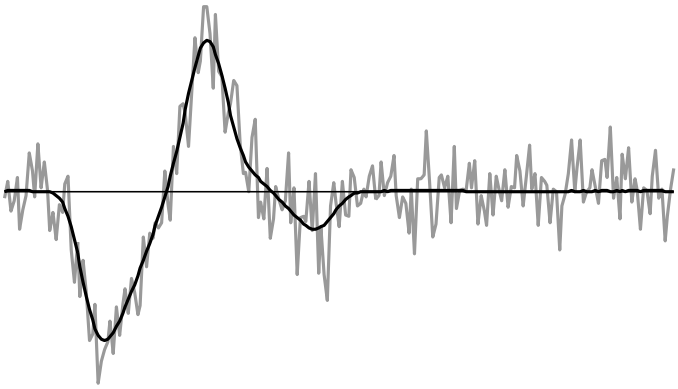

Figure 3. Plot of one of the simulated measuring functionals for one of the detector positions (see the text for details): thick black line represents accurate values and gray line represents the data with added 50% noise.

also be verified by looking at the plot of the cross section of the latter image along the line $x_2 = 0.25$ presented in figure 2.

In order to understand the origins of such unusually low sensitivity to noise, we plot in figure 3 a profile of one of the time series $M_{I_1,B^{(3)}}(y,t)$ for point $y = (1, 0.5, 0.5)$. The thick black line represents the accurate measurements and the gray line represents the data with the added noise. In figure 4, we plot a profile of the reconstructed curl $C^{(1)}(x)$ (gray line) against the correct values (black line). (This plot corresponds to the cross section of the third component of $C^{(1)}$ along the line $x_2 = 0.5$, $x_3 = 0.5$.) The latter figure shows that the noise is amplified during the first step (inversion of the spherical mean Radon transform). This is to be expected since the corresponding inverse problem is mildly ill posed (similar to the classical inverse Radon transform). However, in the second step, corresponding to solving the problem (34), the noise is significantly reduced. This is not surprising since the corresponding operator is a smoothing one. As a result, we obtain the low-noise image shown in figure 1(b).

For the second simulation, we used a phantom of $\ln \sigma$ modeled by a linear combination of slightly smoothed characteristic functions of balls of different radii. The balls were centered on the pairwise intersections of planes $x_1 = 0.25$, $x_2 = 0.25$, and $x_3 = 0.25$ (figure 5).

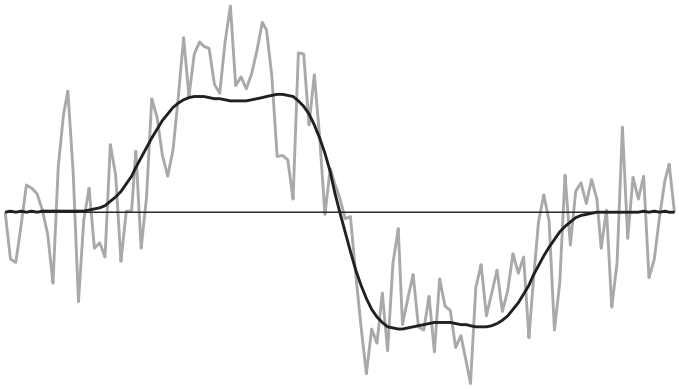

Figure 4. Profile of the reconstructed curl (gray line) compared to the accurate values (thick black line). The values of the third component of $C^{(1)}$ along the line $x_2 = 0.5$, $x_3 = 0.5$ are shown.

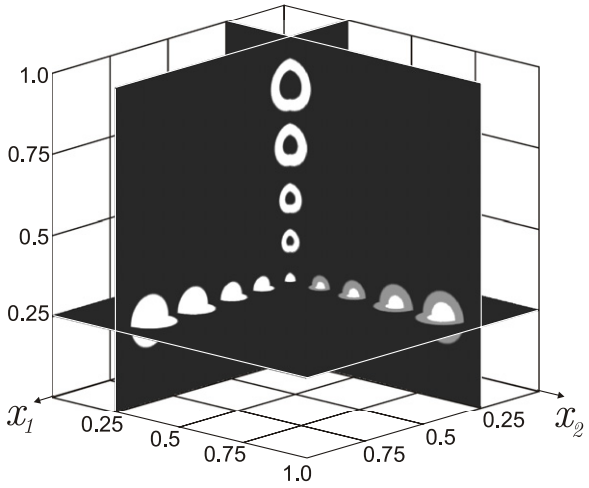

Figure 5. The second (almost) piecewise constant 3D phantom. The cross sections by the planes $x_j = 0.25$, $j = 1, 2, 3$ are shown.

The minimum value of $\ln \sigma$ in this phantom is 0 (black color) and the maximum value is 1 (white color). The simulated data corresponded to the acoustic sources located at the nodes of 257×257 Cartesian grids on each of the six faces of the cubic domain Ω. For each source, time series of 447 values for each measuring functional were simulated. The noise was modeled by adding to each time series a random sequence scaled so that the L^2 norm of the noise was equal to that of the signal.

In figure 6, we shot the graph of $M_{I_1,B^{(3)}}(y,t)$ for the point $y = (1, 0.5, 0.5)$. The black line represents the accurate data; the gray line represents the data with added noise.

The reconstruction was performed on a $257 \times 257 \times 257$ grid. The cross sections of the reconstructed image by the planes $x_1 = 0.25$ and $x_2 = 0.25$ are shown in figures 7(b) and (d), next to the corresponding images of the phantom (i.e. shown in figures 7(a) and (c)). The cross-sectional profile of the image shown in figure 7(d), corresponding to the line $x_1 = 0.25$, $x_3 = 0.25$, is plotted in figure 8.

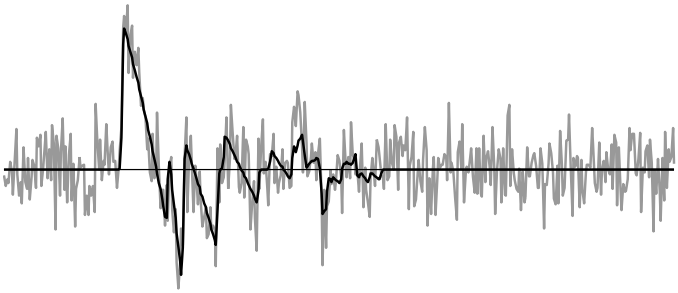

Figure 6. Plot of the values of one of the simulated measurement functionals for one of the detector positions (see the text for details): thick black line represents accurate values and gray line represents the data with added 100% noise.

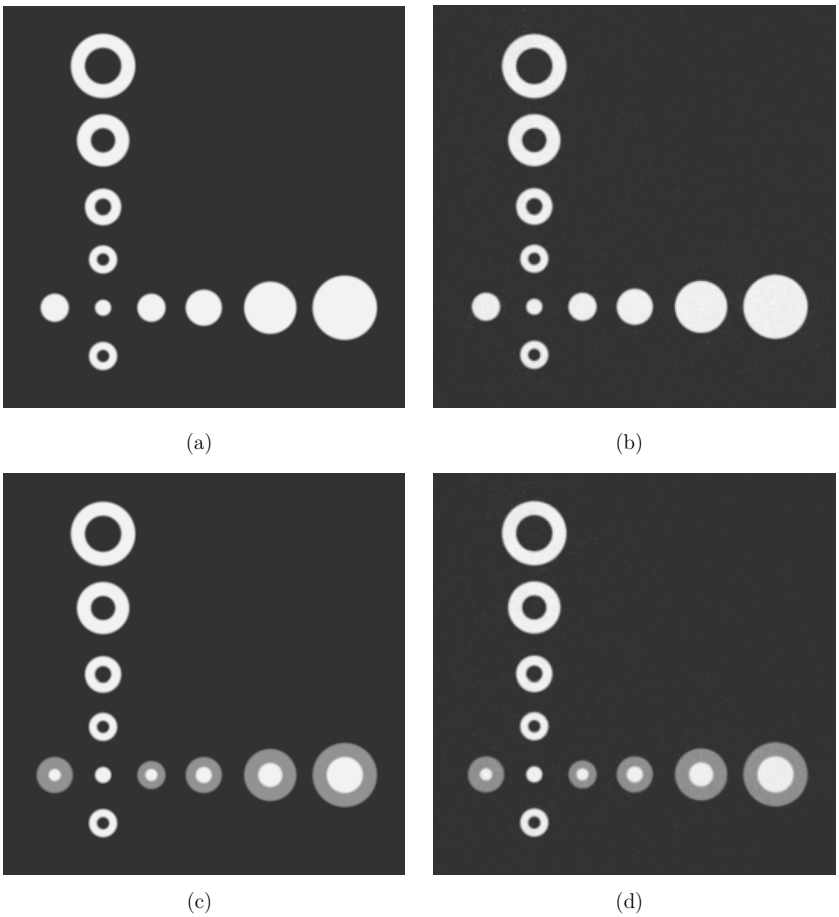

Figure 7. Simulation in 3D with phantom shown in figure 5. (a) and (c) The cross sections of the phantom by the planes $x_2 = 0.25$ and $x_1 = 0.25$, respectively. (b) and (d) The corresponding cross sections of the reconstruction from the data with added 100% (in L_2 sense) noise.

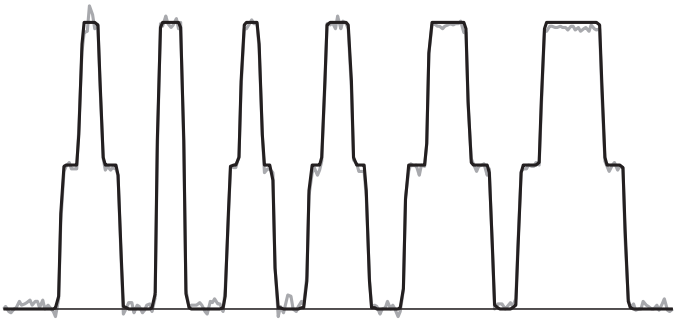

Figure 8. The cross section of the reconstructed image by the line $x_1 = 0.25, x_3 = 0.25$. The thick black line represents the phantom and the gray line corresponds to the image reconstructed from the data with added 100% (in L^2 sense) noise.

As before, we obtained a very accurate reconstruction with little noise. This is again the result of the smoothing, occurring when the Poisson problem is solved in the last step of the algorithm. Additionally, the image benefits from the singular nature of the phantom. While the noise is more or less uniformly distributed over the volume of the cubic domain, the signal (the nonzero $\ln\sigma$) is supported in a rather small fraction of the volume, thus increasing the visual contrast between the noise and the signal.

We have also conducted a third numerical experiment with the same phantom and the same discretization grid as in the second simulation. This time we reconstructed only two curls $C^{(1)}$ and $C^{(2)}$ and, further, computed only currents $J^{(1)}$ and $J^{(2)}$. Instead of using formula (33) at each point of the discretization grid, we solved equations (37)–(39) to obtain $\nabla \ln\sigma$. The rest of the algorithm was the same: compute $\nabla \cdot \nabla \ln\sigma$ and solve the Poisson equation for $\ln\sigma$. The result of the reconstruction was practically indistinguishable from the one shown in figures 7(b) and (d). While the level of noise in the image was slightly higher than in the previous simulation with three currents, it still was remarkably low.

Final remarks and conclusions

Mathematical model

In section 1, we presented a mathematical model of MAET measurements. In general, it agrees with the models [13, 30]. However, instead of pointwise electrical measurements, we consider a more general scheme. The advantage of such an approach is generality and ease of analysis and numerical modeling. It contains as a particular case the pointwise measurement of electrical potentials (as in [13, 30]).

Another novel element in our model is the use of velocity potentials. It simplifies analysis and leads to a better understanding of the problem at hand. We discussed in detail the case of acoustic signal presented by propagating acoustic fronts from small sources. However, the same mathematics can be used to model time-harmonic sources. Since the problem is linear with respect to the velocity potential, the connection between the two problems is through the direct and inverse Fourier transforms of the data in time. Finally, plane wave irradiation (considered, for example, in [30]) is a partial case of irradiation by time-harmonic sources, when they are located far away from the object.

General reconstruction scheme

In sections 2–4, we presented a general scheme for solving the inverse problem of MAET under the assumption of propagating spherical acoustic fronts. (A slight modification of this scheme would allow one to utilize time-harmonic sources and plane waves instead of the fronts we used.) The scheme consists of the following steps.

(i) Apply one of the suitable TAT reconstruction techniques to the measuring functionals $M_{I^{(k)},B^{(j)}}(y,t)$, $j,k=1,2,3$, to reconstruct the regular terms $\frac{\partial}{\partial t}M^{\mathrm{reg}}_{I^{(k)},B^{(j)}}(x,0)$ and, thus, to obtain the curls of $J^{(k)}$.
(ii) Compute currents $J^{(k)}$ from their curls (this step may require one to solve the Neumann problem for the Laplace equation).
(iii) Find $\nabla \ln\sigma$ at each point in Ω using formula (33) or by solving the system of equations (37)–(39).
(iv) Find the values of $\Delta \ln\sigma$ by computing the divergence of $\nabla \ln\sigma$ and compute $\ln\sigma$ by solving the Poisson problem with the zero Dirichlet boundary conditions.

Theoretical properties and numerical methods for all the four steps are well known. The first step is mildly ill posed (similar to the inversion of the classical Radon transform), the second and third steps are stable and the fourth step is described by a smoothing operator. Our rather informal discussion suggests that the total reconstruction procedure is stable (it does not exhibit even the mild instability present in classical computer tomography), and our numerical experiments confirm this assertion. We leave a rigorous proof of this conjecture for future work.

Comparison with AEIT

Similar to AET, MAET overcomes the instability of EIT by combining electrical measurements with ultrasound modulation. However, MAET has some advantages. First, the arising inverse problem is linear and can be solved explicitly. Second, AEIT yields a very weak signal; successful acquisition of AET data in a realistic configuration has not been reported so far. The signal in MAET is stronger and first reconstructions from real data have already been obtained [13].

The case of a rectangular domain

In section 5, we presented a completely explicit set of formulas that yield a series solution of the MAET problem for the case of the cubic domain. It reduces the problem to a set of sine and cosine Fourier transforms and thus can be easily implemented using FFTs. This, in turn, results in a fast algorithm that requires $\mathcal{O}(n^3 \ln n)$ floating-point operations to complete a reconstruction on a Cartesian grid with n^3 nodes.

Feasibility of reconstruction using two directions of B

It is theoretically possible to shorten the potentially long acquisition time by reducing the number of different directions of B. If only two orthogonal directions of the magnetic field B are used, only two components of a curl $C=\nabla\times J_I$ will be reconstructed on the first step of our method (say C_1 and C_2). However, since $\operatorname{div}\operatorname{curl} J=0$,

$$\frac{\partial}{\partial x_3}C_3=-\frac{\partial}{\partial x_1}C_1-\frac{\partial}{\partial x_2}C_2.$$

Since C vanishes on $\partial\Omega$, the above equation can be integrated in x_3, and thus, C_3 can be reconstructed from C_1 and C_2. A further study is needed to see how much this procedure would affect the stability of the whole method.

Acknowledgments

The author gratefully acknowledges the support by the NSF through the grant DMS-0908208. The author is also thankful to anonymous referees for numerous helpful suggestions.

Appendix.

Consider the following system of linear equations:

$$\begin{cases} \mathbf{x}\cdot(\mathbf{a}\times\mathbf{b}) = R_1 \\ \mathbf{x}\cdot(\mathbf{a}\times\mathbf{c}) = R_2 \\ \mathbf{x}\cdot(\mathbf{b}\times\mathbf{c}) = R_3, \end{cases} \tag{A.1}$$

where $\mathbf{a} = (a_1, a_2, a_3)^T$, $\mathbf{b} = (b_1, b_2, b_3)^T$ and $\mathbf{c} = (c_1, c_2, c_3)^T$ are given linearly independent vectors in $\mathbb{R}^3$, $\mathbf{x} = (x_1, x_2, x_3)^T$ is the vector of unknowns and R_1, R_2 and R_3 are given numbers. Equations (A.1) can be re-written in the following form:

$$R_1 = \begin{vmatrix} a_1 & b_1 & x_1 \\ a_2 & b_2 & x_2 \\ a_3 & b_3 & x_3 \end{vmatrix}, \quad R_2 = -\begin{vmatrix} a_1 & x_1 & c_1 \\ a_2 & x_2 & c_2 \\ a_3 & x_3 & c_3 \end{vmatrix}, \quad R_3 = \begin{vmatrix} x_1 & b_1 & c_1 \\ x_2 & b_2 & c_2 \\ x_3 & b_3 & c_3 \end{vmatrix}$$

or

$$v_1 = \frac{1}{\det A}\begin{vmatrix} a_1 & b_1 & x_1 \\ a_2 & b_2 & x_2 \\ a_3 & b_3 & x_3 \end{vmatrix}, \quad v_2 = \frac{1}{\det A}\begin{vmatrix} a_1 & x_1 & c_1 \\ a_2 & x_2 & c_2 \\ a_3 & x_3 & c_3 \end{vmatrix}, \quad v_3 = \frac{1}{\det A}\begin{vmatrix} x_1 & b_1 & c_1 \\ x_2 & b_2 & c_2 \\ x_3 & b_3 & c_3 \end{vmatrix}, \tag{A.2}$$

where A is a matrix whose columns are vectors $\mathbf{a}$, $\mathbf{b}$ and $\mathbf{c}$; $v_j = \frac{R_j(-1)^{j+1}}{\det A}$, $j = 1, 2, 3$. Introduce vectors $\mathbf{R} = (R_3, -R_2, R_1)^T$ and $\mathbf{v} = (v_1, v_2, v_3)^T$. Then, formulas (A.2) can be viewed as the solution of the system of equations $A\mathbf{v} = \mathbf{x}$ obtained using Cramer's rule. Therefore, solution of (A.1) is given by the formula

$$\mathbf{x} = A\mathbf{v} = \frac{1}{\det A}A\mathbf{R} = \frac{1}{\mathbf{a}\cdot(\mathbf{b}\times\mathbf{c})}A\mathbf{R}.$$

References

[1] Agranovsky M and Kuchment P 2007 Uniqueness of reconstruction and an inversion procedure for thermoacoustic and photoacoustic tomography with variable sound speed *Inverse Problems* **23** 2089–102

[2] Ambartsoumian G and Patch S 2007 Thermoacoustic tomography: numerical results *Photons Plus Ultrasound: Imaging and Sensing 2007: The 8th Conference on Biomedical Thermoacoustics, Optoacoustics, and Acousto-optics* vol 6437 ed A A Oraevsky and L V Wang (Bellingham, WA: SPIE Optical Engineering Press) pp 64371B

[3] Ammari H, Bonnetier E, Capdeboscq Y, Tanter M and Fink M 2008 Electrical impedance tomography by elastic deformation *SIAM J. Appl. Math.* **68** 1557–73

[4] Ammari H, Capdeboscq Y, Kang H and Kozhemyak A 2009 Mathematical models and reconstruction methods in magneto-acoustic imaging *Euro. J. Appl. Math.* **20** 303–17

[5] Barber D C and Brown B H 1984 Applied potential tomography *J. Phys. E: Sci. Instrum.* **17** 723–33

[6] Borcea L 2002 Electrical impedance tomography *Inverse Problems* **18** R99–136

[7] Burgholzer P, Matt G J, Haltmeier M and Paltauf G 2007 Exact and approximative imaging methods for photoacoustic tomography using an arbitrary detection surface *Phys Rev.* E **75** 046706

[8] Capdeboscq Y, Fehrenbach J, de Gournay F and Kavian O 2009 Imaging by modification: numerical reconstruction of local conductivities from corresponding power density measurements *SIAM J. Imaging Sci.* **2**/**4** 1003–30
[9] Cheney M, Isaacson D and Newell J C 1999 Electrical impedance tomography *SIAM Rev.* **41** 85–101
[10] Colton D and Kress R 2001 *Inverse Acoustic and Electromagnetic Scattering Theory* (Berlin: Springer)
[11] Finch D, Patch S and Rakesh 2004 Determining a function from its mean values over a family of spheres *SIAM J. Math. Anal.* **35** 1213–40
[12] Gilbarg D and Trudinger N S 1983 *Elliptic Partial Differential Equations of Second Order* (Berlin: Springer)
[13] Haider S, Hrbek A and Xu Y 2008 Magneto-acousto-electrical tomography: a potential method for imaging current density and electrical impedance *Physiol. Meas.* **29** S41–50
[14] Hristova Y, Kuchment P and Nguyen L 2008 On reconstruction and time reversal in thermoacoustic tomography in homogeneous and non-homogeneous acoustic media *Inverse Problems* **24** 055006
[15] Kruger R A, Liu P, Fang Y R and Appledorn C R 1995 Photoacoustic ultrasound (PAUS) reconstruction tomography *Med. Phys.* **22** 1605–09
[16] Kruger R A, Reinecke D R and Kruger G A 1999 Thermoacoustic computed tomography: technical considerations *Med. Phys.* **26** 1832–7
[17] Kuchment P and Kunyansky L 2011 Mathematics of photoacoustic and thermoacoustic tomography *Handbook of Mathematical Methods in Imaging* (Berlin: Springer) chapter 19 pp 819–65
[18] Kuchment P and Kunyansky L 2010 Synthetic focusing in ultrasound modulated tomography *Inverse Problems Imaging* **4** 665–73
[19] Kuchment P and Kunyansky L 2011 2D and 3D reconstructions in acousto-electric tomography *Inverse Problems* **27** 055013
[20] Kunyansky L 2007 Explicit inversion formulae for the spherical mean Radon transform *Inverse Problems* **23** 737–83
[21] Kunyansky L 2007 A series solution and a fast algorithm for the inversion of the spherical mean Radon transform *Inverse Problems* **23** S11–20
[22] Kunyansky L 2011 Reconstruction of a function from its spherical (circular) means with the centers lying on the surface of certain polygons and polyhedra *Inverse Problems* **27** 025012
[23] Kunyansky L 2012 Fast reconstruction algorithms for the thermoacoustic tomography in certain domains with cylindrical or spherical symmetries *Inverse Problems Imaging* at press (arXiv:1102.1413)
[24] Kunyansky L and Kuchment P 2010 Synthetic focusing in acousto-electric tomography *Oberwolfach Report* No. 18/2010 (Workshop on Mathematics and Algorithms in Tomography, organized by Martin Burger, Alfred Louis and Todd Quinto) pp 44–47
[25] Lavandier B, Jossinet J and Cathignol D 2000 Experimental measurement of the acousto-electric interaction signal in saline solution *Ultrasonics* **38** 929–36
[26] Montalibet A, Jossinet J, Matias A and Cathignol D 2001 Electric current generated by ultrasonically induced Lorentz force in biological media *Med. Biol. Eng. Comput.* **39** 15–20
[27] Norton S J and Linzer M 1981 Ultrasonic reflectivity imaging in three dimensions: exact inverse scattering solutions for plane, cylindrical and spherical apertures *IEEE Trans. Biomed. Eng.* **28** 200–2
[28] Nguyen L 2009 A family of inversion formulas in thermoacoustic tomography *Inverse Problems Imaging* **3** 649–75
[29] Oraevsky A A, Jacques S L, Esenaliev R O and Tittel F K 1994 Laser-based photoacoustic imaging in biological tissues *Proc. SPIE* **2134A** 122–8
[30] Roth B J and Schalte K 2009 Ultrasonically-induced Lorentz force tomography *Med. Biol. Eng. Comput.* **47** 573–7
[31] Stewart A M 2008 Longitudinal and transverse components of a vector field *Classical Physics* in press (arXiv: 0801.0335v2)
[32] Vladimirov V S 1971 *Equations of Mathematical Physics Pure and Applied Mathematics* vol 3 ed A Jeffrey (New York: Marcel Dekker)
[33] Wang L V (ed) 2009 *Photoacoustic Imaging and Spectroscopy* (Boca Raton, FL: CRC Press)
[34] Wen H, Shah J and Balaban R S 1998 Hall effect imaging *IEEE Trans. Biomed. Eng.* **45** 119–24
[35] Xu M and Wang L-H V 2002 Time-domain reconstruction for thermoacoustic tomography in a spherical geometry *IEEE Trans. Med. Imag.* **21** 814–22
[36] Zhang H and Wang L 2004 Acousto-electric tomography *Proc. SPIE* **5320** 145–9